Available online at www.sciencedirect.com
ScienceDirect
Trans. Nonferrous Met. Soc. China 32(2022) 2243−2252
Transactions of Nonferrous Metals Society of China
www.tnmsc.cn

Influence of anions in phosphate and tetraborate electrolytes on growth kinetics of microarc oxidation coatings on Ti6Al4V alloy

Xiao-ming WANG[1,2,3], Fu-qin ZHANG[1]

1. Powder Metallurgy Research Institute, Central South University, Changsha 410083, China;
2. Department of Mechanical and Energy Engineering, Shaoyang University, Shaoyang 422000, China;
3. Key Laboratory of Hunan Province for Efficient Power System and Intelligent Manufacturing, Shaoyang University, Shaoyang 422000, China

Received 21 July 2021; accepted 2 December 2021

Abstract: The growth kinetics of microarc oxidation (MAO) coatings on Ti6Al4V alloy was studied by designing an electrolyte with low PO_4^{3-} content and high $B_4O_7^{2-}$ content, using scanning electron microscopy, transmission electron microscopy, X-ray diffraction, and potentiodynamic polarization. The results showed that $B_4O_7^{2-}$ increased the spark intensity and dissolved most of the oxides at high temperatures. Then, a thicker barrier layer at the coating/substrate interface was produced, which increased the polarization resistance of the coating. PO_4^{3-} at a low concentration also promoted the uniform growth of the MAO coating and the formation of hat-shaped holes in the outer deposition layer. The thickness of the MAO coatings obtained in $Na_2B_4O_7$ electrolytes exhibited an exponential increase with time at spark discharge stage, while that of the MAO coating obtained in phosphate–tetraborate electrolytes showed a linear trend as the PO_4^{3-} content increased.

Key words: Ti6Al4V alloy; microarc oxidation; phosphate; tetraborate; electrolyte; anions; growth kinetics

1 Introduction

Titanium and titanium alloys are perfect bioengineering materials because of their high specific strength, ductility, corrosion resistance, and bioinertness. They are especially suitable for internal use in the human body [1]. However, titanium and titanium alloys still have some disadvantages in biomedical applications, such as poor osseointegration due to their bioinertness, and poor biocompatibility due to bacterial infection or the release of metal elements [2−4]. A variety of surface activation techniques including sol−gel [5], PVD [6], hydrothermal [7], and cold spray [8] were used to modify the titanium implant surface. Nevertheless, the coatings formed by these processes have some defects such as low fatigue strength, high residual stress and weak adhesion to the metal matrix [9]. Microarc oxidation (MAO), also known as the plasma electrolytic oxidation, is a relatively new surface modification technology that was developed from anodic oxidation. A MAO ceramic coating creates a dense barrier layer, which significantly improves corrosion resistance and prevents the release of toxic elements (such as Al and V) in titanium alloys, thus improving their biocompatibility [10,11]. Moreover, the MAO of titanium and its alloys can form a porous and rough surface structure, which is beneficial to the formation and integration of new bone [12,13].

During the MAO process, the metal is oxidized with an electron avalanche, and the key challenge is whether the electric field of the residual oxide layer can reach the necessary level of dielectric breakdown. Research from multiple

Corresponding author: Fu-qin ZHANG, E-mail: zhangfuqin@csu.edu.cn
DOI: 10.1016/S1003-6326(22)65944-2

groups has shown that the transfer behavior of ions in the MAO coating is a critical component of this issue [10]. MATYKINA et al [14] used ^{18}O as a tracer during MAO treatment, which revealed that the oxygen in the MAO coating originated from the water of the electrolyte. GAO et al [15] conducted MAO treatment to consume an aluminum film coated on a Ti substrate, and found that the molten oxide of Ti is formed by discharge and ejects the discharge channel. MORTAZAVI et al [16] carried out MAO treatment on pure titanium in a phosphate electrolyte and found that the crystallization area in the middle of the MAO coating did not contain any phosphorous, while a small amount of phosphorous was found in the amorphous area at the top of the MAO coating. However, AO et al [17] conducted MAO on titanium alloy in a phosphate/silicate electrolyte, and detected some phosphorus at the coating/substrate interface. It follows that the distribution of phosphorus deposited in the coating is controversial, and a fixed concentration of electrolyte containing phosphate cannot well reveal the role of PO_4^{3-} ions on the mechanism of the growth of MAO coatings. Furthermore, RUDNEV et al [18] revealed that $B_4O_7^{2-}$ ions can react with molten titanium dioxide that has erupted by microarc discharge and penetrate the coordination sphere of the Ti^{4+} hydroxide complexes in the electrolyte, forming a coating with a different morphology and composition obtained from other electrolytes. Therefore, it is difficult to explain the dynamic growth behavior of the MAO coating formed on titanium alloys in borate electrolytes based on the proposed linear or exponential growth models [19,20], and there are few reports on the mechanism of $B_4O_7^{2-}$ on the growth of MAO coatings.

Herein, bivariate electrolytes of sodium phosphate and sodium borate with different ratios of PO_4^{3-} and $B_4O_7^{2-}$ ions were used for the MAO of Ti6Al4V alloy. The surface morphology, composition, and properties of the MAO coatings formed were examined to investigate the effect of PO_4^{3-} and $B_4O_7^{2-}$ ions on the MAO film growth mechanism.

2 Experimental

MAO experiments were performed on samples of *d*10 mm rods in size that were cut from a bar of Ti6Al4V alloy (Baoji Titanium Industry Co., Ltd., China). The nominal composition (mass fraction) of the Ti alloy was 0.141% Fe, 0.008% H, 0.13% O, 6.43% Al, 4.13% V, and balanced Ti. The MAO was carried out using pulsed electrical power (ANS Power Supply Co., Ltd., China) at 5 A/dm^2. The pulse frequency and duty cycle were set to be 200 Hz and 10%, respectively. The electrolyte temperature was kept below 30 °C by a heat exchange system during the MAO process. The $Na_3PO_4/Na_2B_4O_7$ (P/B) electrolyte was prepared from $Na_3PO_4·12H_2O$ and $Na_2B_4O_7·5H_2O$ (Chron Chemicals Co., Ltd., China) at a total electrolyte concentration of 0.1 mol/L. To determine the effect of the proportion of the components in the P/B electrolyte on the MAO coating, the experiment was divided into three groups as shown in Table 1. Process time of 30, 240, 400, 600, 960, 1200, and 1800 s was selected to investigate the growth kinetics of MAO coatings.

Table 1 Proportions of components in P/B electrolytes

Sample	$Na_2B_4O_7$ concentration/ (mol·L^{-1})	Na_3PO_4 concentration/ (mol·L^{-1})	Molar fraction of PO_4^{3-}/%
B10	0.1	0	0
P1B9	0.09	0.01	10
P1.5B8.5	0.015	0.085	15

The surface and cross-sectional morphology of the MAO coatings were observed by scanning electron microscopy (SEM, Phenom ProX, Funa Scientific Instrument (Shanghai) Co., Ltd., China) and transmission electron microscopy (TEM, JEM−2100F, JEOL Co., Ltd., Japan). The distribution of Ti, O, Al, Si, and P was determined by energy dispersive spectrometry (EDS, Phenom ProX, Funa Scientific Instrument (Shanghai) Co., Ltd., China). The thickness of the MAO coatings was determined by a coating thickness gauge (DUALSCOPE MP0, Fischer, Germany). Cu K_α radiation was used at 40 kV and 30 mA over a 2θ range from 10° to 90° with a scan speed of 0.1 (°)/s to analyze the phase composition of the coatings by X-ray diffraction (XRD, AL−2700B, Dandong Aolong Radiative Instrument Group Co., Ltd., China). The phase composition of the coatings was quantitatively analyzed by the adiabatic method. The adiabatic method is based on the theory that the

peak intensity of a particular phase in a phase mixture is proportional to its mass fraction [21]. According to this theory, if there are N phases in a system, the mass fraction of phase i can be calculated using Eq. (1):

$$w_i = I_i \Big/ K_j^i \sum_{i=1}^{N} \left(I_i / K_j^i \right) \tag{1}$$

where w_i is the mass fraction of phase i in the sample, I_i is the strongest diffraction peak intensity of phase i, and K_j^i is the intensity ratio of the strongest diffraction peak of reference phase j to phase i (1:1 mixing). Potentiodynamic polarization curves of the samples obtained in different electrolytes were recorded in a 3.5 wt.% NaCl solution using a CS120 electrochemical measurement system (CS120, Wuhan Corrtest Instruments Corp., Ltd., China) at a scan rate of 0.1 mV/s from −0.4 to 0.2 V. All samples were immersed in the test solution for 4 h prior to the test to attain a stable open circuit potential (OCP). OCP measurements were conducted every 5 min throughout the 4 h immersion time.

3 Results and discussion

3.1 Evolution of MAO process voltage

The process voltage of the Ti6Al4V alloy treated by MAO in P/B electrolyte is shown in Fig. 1. According to different voltage growth rates, the MAO process had the following three stages. Stage I (anodic oxidation stage) had the fastest voltage growth rate and was linear, and in this stage, there were many bubbles but no sparks. When the anodizing process exceeded 7 s, weak sparks and a hiss produced by discharge appeared on the surface of the sample and the voltage growth rate decreased, indicating that the anodized film was broken down. In all three groups of electrolytes, the breakdown voltages of the anodized films on the titanium alloy reached approximately 152 V, indicating that the electrolyte had negligible effect on the anodic oxidation process. In Stage II (spark discharge stage), the process voltage increased exponentially, and there were many bubbles and sparks. As the proportion of PO_4^{3-} in the electrolyte increased, the process voltage increased significantly but the time spent in Stage II gradually shortened. In Stage III (microarc discharge stage), the voltage increased relatively slowly and linearly, and there were many bubbles and some bright microarcs. The process voltage in the B10 electrolyte generally increased very slowly, but a small amount of PO_4^{3-} improved the voltage growth rate significantly, as seen by the process voltage in the P1.5B8.5 electrolyte, which surprisingly increased sharply during MAO from 400 to 800 s.

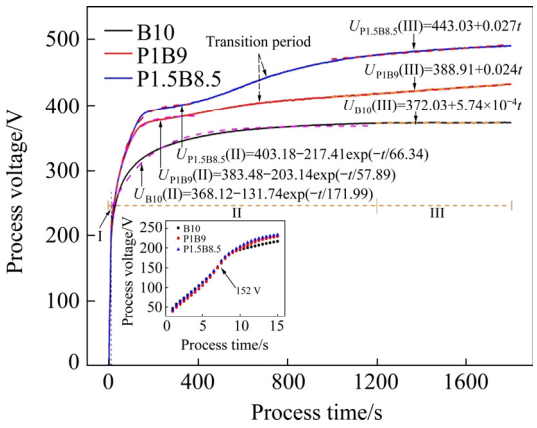

Fig. 1 Process voltage of Ti6Al4V alloy treated by MAO in P/B electrolyte

3.2 Evolution of structural characteristics of MAO coating

Figure 2 shows the surface morphologies of the MAO coating obtained in the P/B electrolyte. At 30 s of processing, the surface of the titanium alloy in the B10 electrolyte was still smooth, although there were some discharge pores with diameters of ~0.5 μm and a few worm-like discharge channels with lengths of ~2 μm (Fig. 2(a)). Many micro pores with diameters of 0.5−1 μm appeared on the surface of titanium alloy in the P/B electrolyte, and some residual oxides were deposited around them (see Figs. 2(b) and (c)). When the process reached 240 s in the B10 electrolyte, micropores with diameters of ~0.5 μm spread throughout the surface of the titanium alloy, and a small number of relatively large pores (~1 μm in diameter) appeared in local areas; whereas at 240 s in the P1B9 and P1.5B8.5 electrolytes, many relatively large pores (1−2 μm in diameter) appeared on the surface of the titanium alloy. As the process continued to 1800 s, the micropores on the surface of the titanium alloy in the B10 electrolyte grew slowly, but the relatively large pores formed by concentrated discharge in local areas (also called “cascade” discharge [22,23]) increased rapidly, reaching 2−5 μm in diameter. Some molten oxides remained

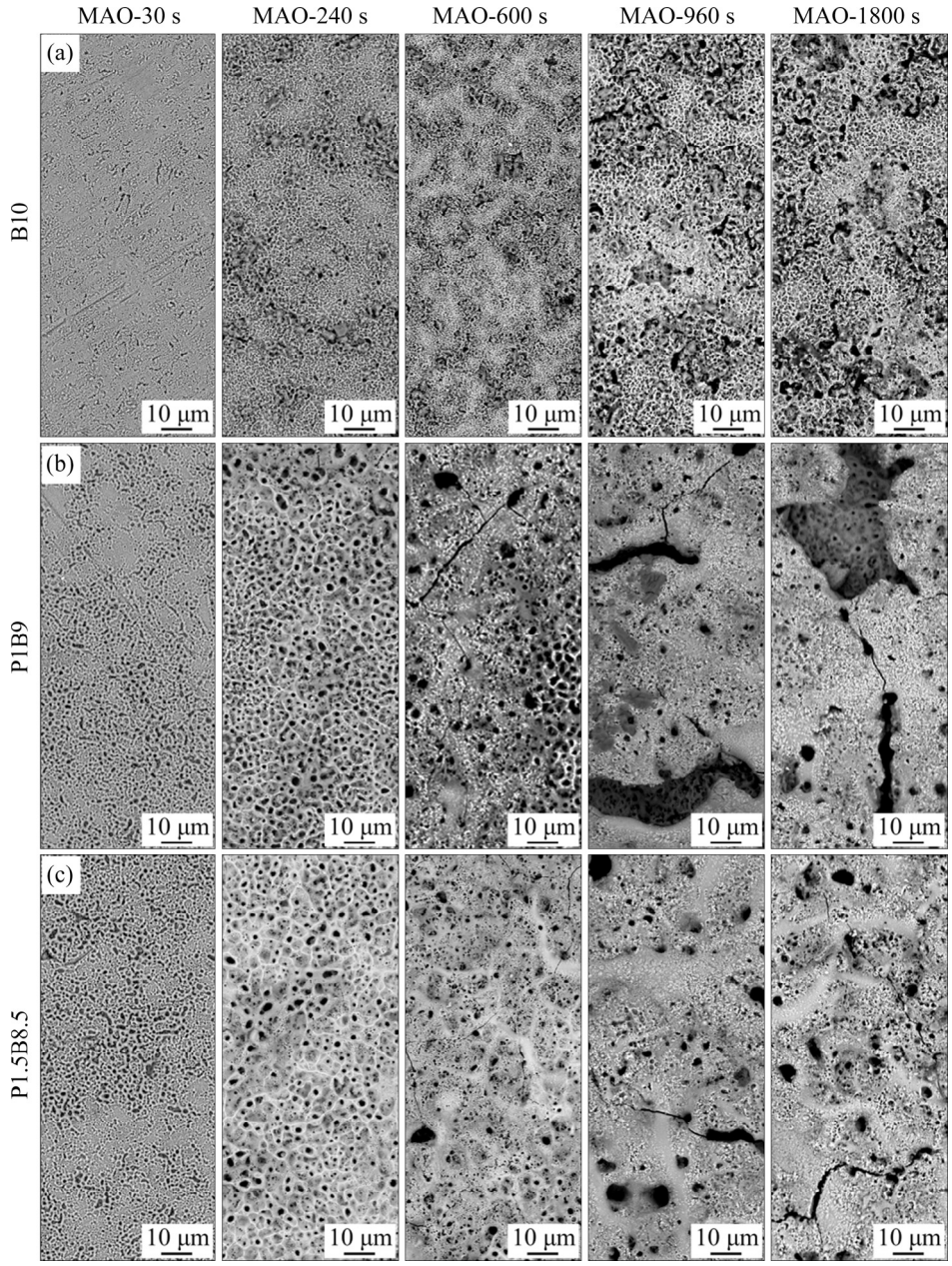

Fig. 2 Surface morphologies of MAO coatings obtained in B10 (a), P1B9 (b) and P1.5B8.5 (c) electrolytes

on the surface of the titanium alloys in the P1B9 and P1.5B8.5 electrolytes, forming an outer deposition layer, and huge discharge pits (50−100 μm in length) were found on the surface of the titanium alloy in the P1B9 electrolyte.

The cross-sectional morphologies of the coatings obtained at 1800 s in P/B electrolytes are shown in Fig. 3. As shown in Fig. 3(a), the coating obtained in the B10 electrolyte was thin (~5 μm), and the interface between the coating and titanium alloy exhibited a zigzag profile, which was caused by the cascade discharge. A dense oxide layer with a thickness of ~0.6 μm was evident at the interface between the coating and the titanium alloy, which is usually called the barrier layer. EDS results of surface mapping scanning (Fig. 4) and cross-sectional line-scanning indicated that a small amount of boron was detected on the surface of the MAO coating obtained in B10 electrolyte. As shown in Figs. 3(b) and (c), the coatings obtained in the P1B9 and P1.5B8.5 electrolytes were relatively thick (40−50 μm), and the interface between the coating and titanium alloy was relatively smooth. Some hat-shaped holes formed by discharge were found in the MAO coating, and some of these holes were connected, causing the outer deposition layer

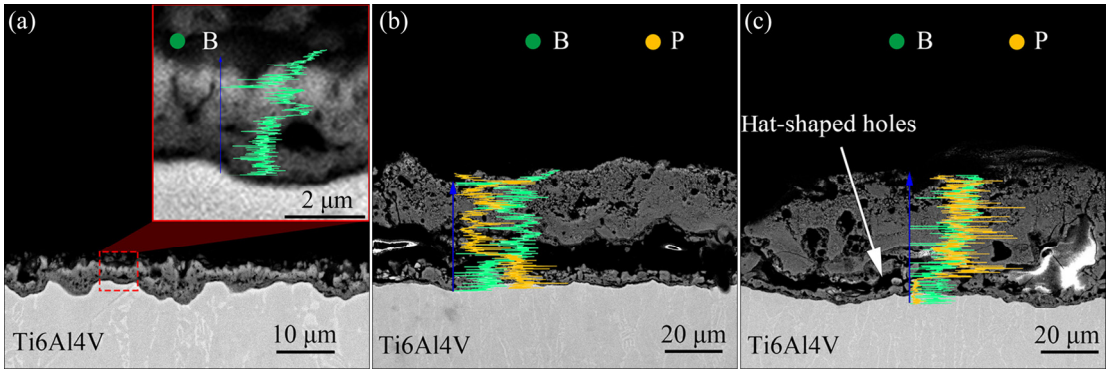

Fig. 3 Cross-sectional morphologies and corresponding element distribution of MAO coatings obtained at 1800 s in B10 (a), P1B9 (b) and P1.5B8.5 (c) electrolytes

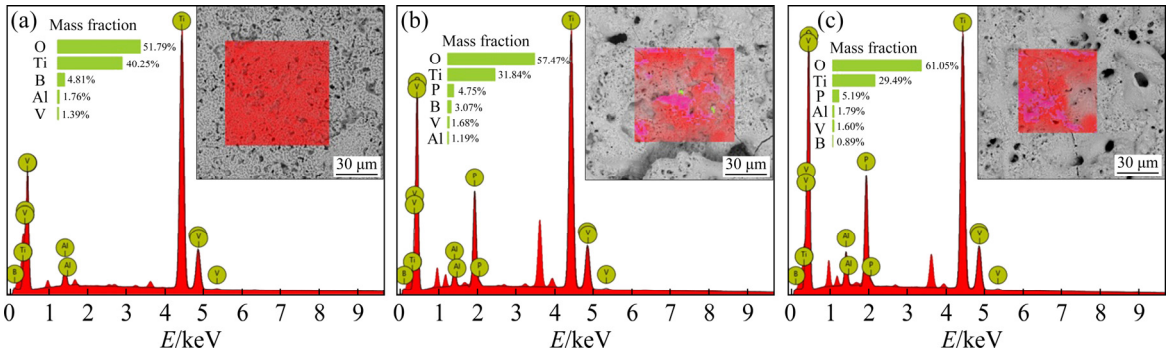

Fig. 4 Element mapping of MAO coatings obtained at 1800 s in B10 (a), P1B9 (b) and P1.5B8.5 (c) electrolytes

to have peeled off. EDS analysis showed that very little boron was detected on the surface of the MAO coating obtained in the P1B9 and P1.5B8.5 electrolytes, while relatively more boron was detected in the hat-shaped holes.

The XRD patterns of the coated samples at 1800 s in P/B electrolytes are shown in Fig. 5, and the phase contents were quantitatively analyzed by the adiabatic method [21] and are shown in Table 2. The MAO coating obtained in the B10 electrolyte contained a large amount of rutile phase, while the amount of anatase phase was negligible. The MAO coatings obtained in the P1B9 and P1.5B8.5 electrolytes contained both anatase and rutile phases, but the MAO coating obtained in the P1.5B8.5 electrolyte contained slightly more anatase phase than the one obtained in the P1B9 electrolyte. Generally, the higher the PO_4^{3-} content in the electrolyte was, the more the anatase phase was produced.

Figure 6 shows the TEM bright-field images and selected area diffraction patterns of the MAO coatings. After 1800 s in B10 electrolyte, some filamentous discharge channels were found in the

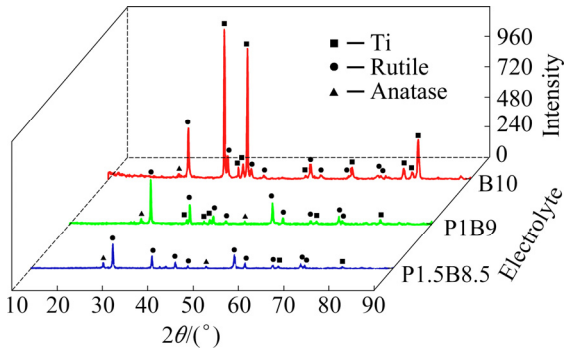

Fig. 5 XRD patterns of MAO coatings obtained at 1800 s in B10, P1B9 and P1.5B8.5 electrolytes

Table 2 Contents of phases during MAO process (wt.%)

Sample	Rutile	Anatase	Ti
B10	17.26	0.98	81.76
P1B9	77.34	5.47	17.19
P1.5B8.5	80.34	10.55	9.11

inner layer of the MAO coating (Fig. 6(a)), which promoted cascade discharge; the high magnification image and the selected area diffraction patterns showed that there were some rutile nanocrystallines

and amorphous phases surrounding the filamentous channels.

For the MAO coating obtained after 1800 s in P1.5B8.5 electrolyte, many pores but no filamentous channels were observed in the inner layer. In addition, some amorphous phase material surrounded the pores (Fig. 6(b)), indicating that PO_4^{3-} is beneficial to the formation of the amorphous phase as well as pores in the MAO coating. The MAO coating contained both anatase and rutile phases. Generally, low PO_4^{3-} content caused the filamentous channels to be blocked by the molten oxide, which promoted the generation of secondary discharge around the channel, so the cascade discharge phenomenon was avoided during the MAO process at low PO_4^{3-} content.

3.3 Potentiodynamic polarization characteristics of MAO coating

The potentiodynamic polarization curves of the MAO coatings in a 3.5% NaCl solution obtained in different electrolytes are shown in Fig. 7. The Tafel constants (β_a and β_c), corrosion rate (v_{corr}), and corrosion current density (J_{corr}) were derived from the data by Tafel extrapolation. The polarization resistance (R_p) was calculated according to the Stern−Geary equation [24] and is presented in Table 3. The MAO coating obtained in the B10 electrolyte had higher polarization resistance than the MAO coatings obtained in the P1B9 and P1.5B8.5 electrolytes, although the B10 electrolyte coating is thin and contains some filamentation channels. This is because $B_4O_7^{2-}$ significantly promotes the growth of microarc intensity, and the dense inner barrier layer can be obtained. Generally, the thicker the barrier layer formed by microarc discharge between the coating and substrate is, the better the corrosion resistance of the MAO coating is, while the outer deposition layer had little effect on the corrosion resistance of the MAO coating because of its many hat-shaped holes and cracks.

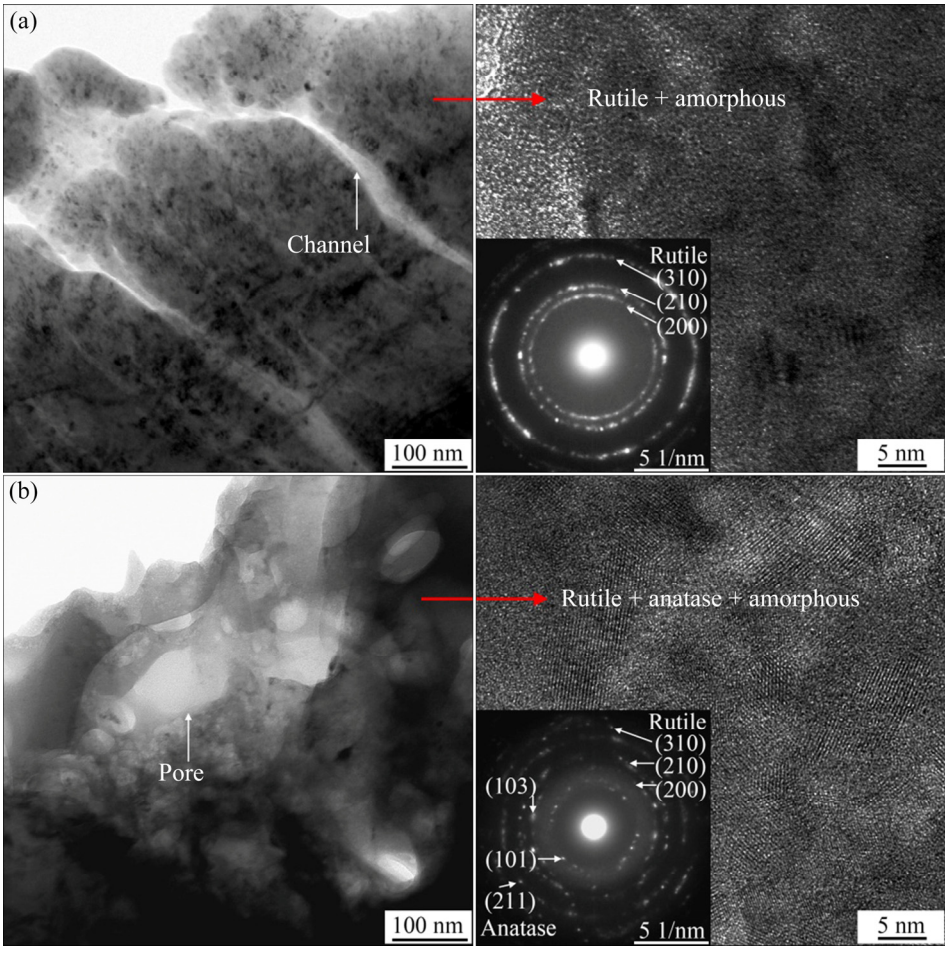

Fig. 6 TEM bright-field image, high magnification image and selected area diffraction patterns of inner layer of MAO coatings obtained in B10 (a) and P1.5B8.5 (b) electrolytes

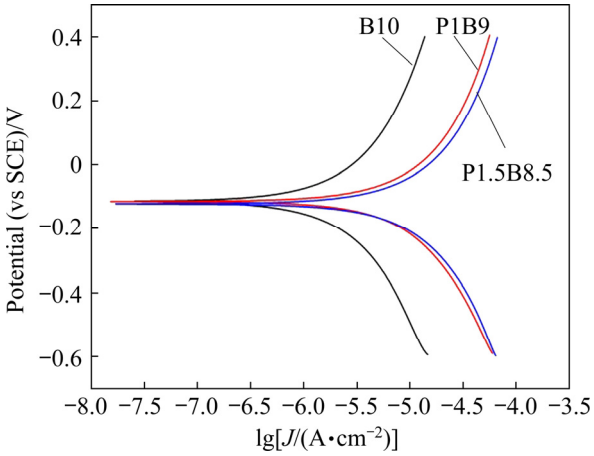

Fig. 7 Potentiodynamic polarization curves of MAO coatings obtained at 1800 s in 3.5% NaCl solution

Table 3 Potentiodynamic polarization data of MAO coatings obtained at 1800 s in 3.5% NaCl solution

Sample	β_a/ (mV·dec^{-1})	β_c/ (mV·dec^{-1})	J_{corr}/ (μA·cm^{-2})	v_{corr}/ (mm·A^{-1})	R_p/ (kΩ·cm^2)
B10	1952.2	1919.1	0.0105	0.0916	39.975
P1B9	1354.9	1789.0	0.0341	0.297	9.830
P1.5B8.5	1008.6	1142.8	0.0275	0.244	8.446

3.4 Growth kinetics of MAO coatings

The variations in thickness of the MAO coatings with process time obtained in the P/B electrolytes are shown in Fig. 8. In Stage II, the coating thickness (H(II)) exhibited an exponential increase with the increase of the time (t), and the growth of the coating can be described by the following equation:

$$H(\mathrm{II}) = a - b\exp(-t/c) \quad (2)$$

where a, b, and c are constants related to the experimental parameters. As the $B_4O_7^{2-}$ content in the electrolyte decreased, the constants a and b tended to become equal and the constant c became large. The growth of the MAO coating showed a linear trend when the constant c was large. It then follows that the thickness of the MAO coating, by its nature, increases linearly. However, the above results show that the thickness of MAO coating increases exponentially because of the dissolution of the molten oxide by the electrolyte rather than defects in the substrate [25]. A good explanation for the linear growth of the MAO coating in sodium phosphate electrolyte and the parabolic (or exponential) growth in sodium borate electrolyte has been previously proposed [3,26]. In Stage III, the coating thickness (H(III)) exhibited a linear increase with the increase of time, which is consistent with observations in other studies [27−29]. The growth of the coating is described by the following equation:

$$H(\mathrm{III}) = H_0 + kt \quad (3)$$

where H_0 is the final thickness of the MAO coating obtained in Stage II, and parameter k is related to the dissolution rate and production rate of molten oxides. The production rate of molten oxides gradually reaches an equilibrium with the dissolution rate as the spark intensity increases, so k is a constant in Stage III. There is, of course, a transitional period before that.

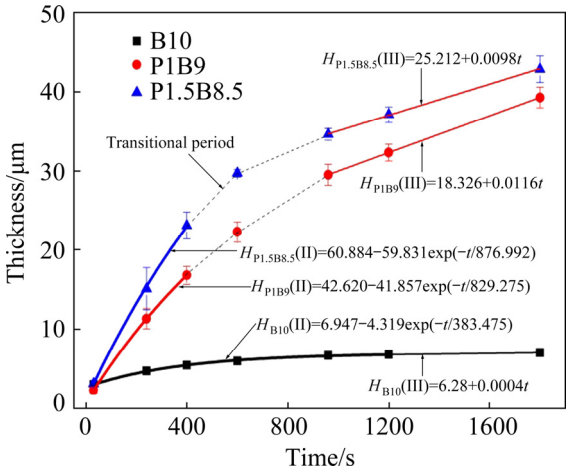

Fig. 8 Thickness of MAO coating obtained in P/B electrolytes

A growth kinetics mechanism of the MAO coatings was proposed, which encompasses the above analyses of process voltage, surface morphology, cross-sectional morphology, phase composition, and corrosion resistance of the MAO coatings. Figure 9 shows a schematic diagram of the growth of the MAO coatings obtained in P/B electrolytes. In B10 electrolyte, as shown in Fig. 9(a), sparks first occur at the defect grains on the surface of the titanium alloy. Because the small amount of molten oxide produced by the discharge is completely dissolved by $B_4O_7^{2-}$ [3,30], and the ion channels in the coating are still unblocked, many sparks will be at or around the defect grain. At the end of Stage II, the first inner layer without residual oxides (hereinafter referred to as "inner deposition layer") completely covers the surface of

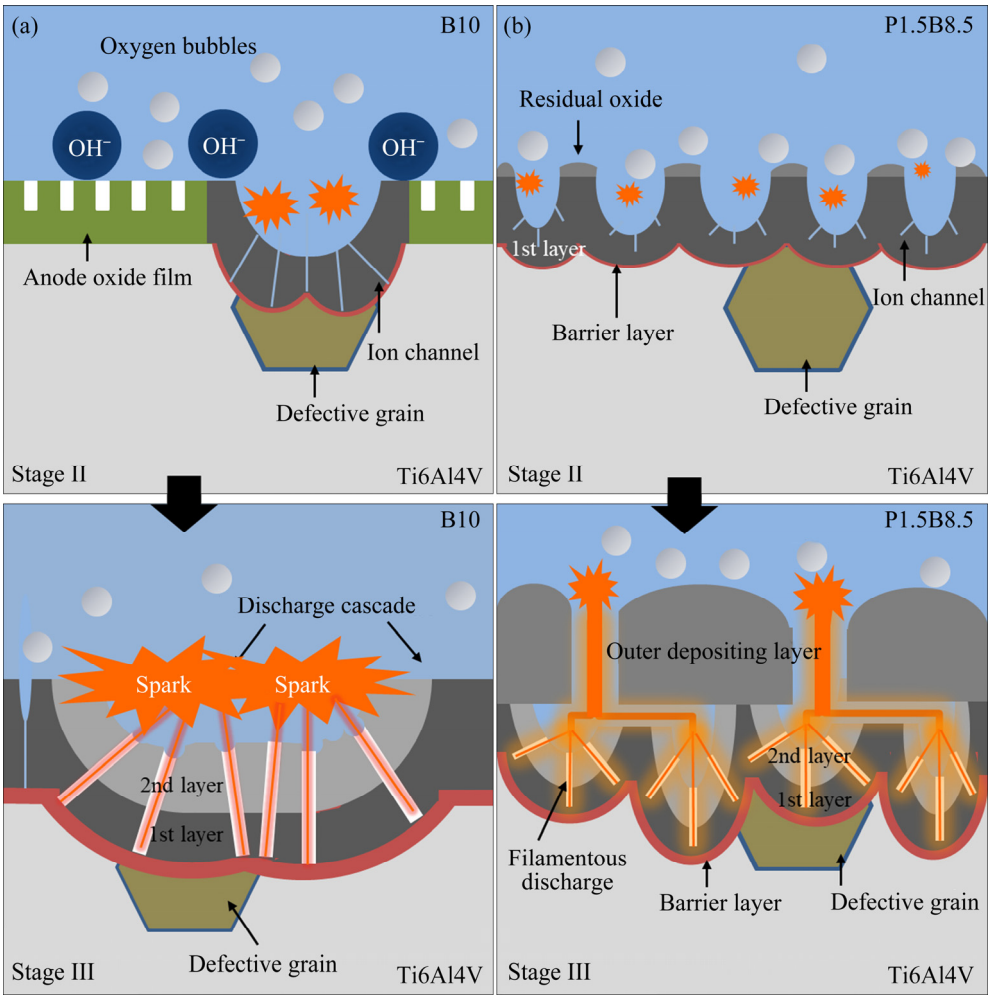

Fig. 9 Schematic diagrams of growth of MAO coating obtained in B10 (a) and P1.5B8.5 (b) electrolytes

the sample. In Stage III, microarc discharges are again generated around the defective grains, and a cascade discharge is formed. Strong cascade discharges form a dense and thick barrier layer at the coating/substrate interface, which significantly improves its corrosion resistance (Fig. 7), but severe cascade discharges may damage the integrity of the coating. Finally, the coating/substrate interface forms a zigzagged profile under cascade discharge action. In P1.5B8.5 electrolyte, as shown in Fig. 9(b), sparks were distributed uniformly on the surface of the titanium alloy without the discharge concentration phenomenon. This can be explained by the fact that the residual molten oxide produced by the first discharge blocks the ion channels in the coating (Fig. 6), causing the secondary discharge to transfer to other areas [31]. Therefore, the first inner deposition layer and the first outer deposition layer are obtained in Stage II. In Stage III, the filamentous sparks originating in the inner deposition layer are concentrated in the outer deposition layer, and some molten oxides accumulate on the surface of the sample while many hat-shaped holes are formed in the coating.

Based on the growth kinetics mechanism of the MAO coatings in the P/B electrolytes, it is of great significance to provide a scientific theoretical basis for the design of MAO coating with complex functions. For example, an electrolyte with high $B_4O_7^{2-}$ content can be used to design porous hydrophilic coating, and a small amount of PO_4^{3-} can be added into the electrolyte to eliminate the damage of the biological coating caused by cascade discharge.

4 Conclusions

(1) $B_4O_7^{2-}$ increased the spark intensity and dissolved most of the molten oxides, and a thicker barrier layer at the coating/substrate interface was produced, resulting in higher polarization resistance of the coating.

(2) PO_4^{3-} with low content promoted the uniform growth of the MAO coating and the formation of hat-shaped holes under the outer deposition layer.

(3) During spark discharge stage, the thickness of the MAO coatings obtained in $Na_2B_4O_7$ electrolytes exhibited an exponential increase with the increase of time, while the growth of the MAO coating obtained in P/B electrolytes showed a linear trend as the PO_4^{3-} content increased.

References

[1] ZHAI Da-jun, FENG Ke-qin. Preparation of micro/nano-structured ceramic coatings on Ti6Al4V alloy by plasma electrolytic oxidation process [J]. Transactions of Nonferrous Metals Society of China, 2019, 29(12): 2546−2555.

[2] GOGHERI M S, KASIRI-ASGARANI M, BAKHSHESHI-RAD H R, GHAYOUR H, RAFIEI M. Mechanical properties, corrosion behavior and biocompatibility of orthopedic pure titanium−magnesium alloy screw prepared by friction welding [J]. Transactions of Nonferrous Metals Society of China, 2020, 30(11): 2952−2966.

[3] ZHAI Da-jun, FENG Ke-qin, YUE Hui-fang. Growth kinetics of microarc oxidation TiO_2 ceramic film on Ti_6Al_4V alloy in tetraborate electrolyte [J]. Metallurgical and Materials Transactions A, 2019, 50(5): 2507−2518.

[4] YIGIT O, DIKICI B, OZDEMIR N, ARSLAN E. Plasma electrolytic oxidation of Ti−6Al−4V alloys in nHA/GNS containing electrolytes for biomedical applications: The combined effect of the deposition frequency and GNS weight percentage [J]. Surface and Coatings Technology, 2021, 415: 127139.

[5] DIKICI B, NIINOMI M, TOPUZ M, KOC S G, NAKAI M. Synthesis of biphasic calcium phosphate (BCP) coatings on β-type titanium alloys reinforced with rutile-TiO_2 compounds: Adhesion resistance and in-vitro corrosion [J]. Journal of Sol−Gel Science and Technology, 2018, 87: 713−724.

[6] ZARKA M, DIKICI B, NIINOMI M, EZIRMIK K V, NAKAI M, YILMAZER H. A systematic study of β-type Ti-based PVD coatings on magnesium for biomedical application [J]. Vacuum, 2021, 183: 109850.

[7] YIGIT O, DIKICI B, SENOCAK T C, OZDEMIR N. One-step synthesis of nano-hydroxyapatite/graphene nano-sheet hybrid coatings on Ti6Al4V alloys by hydrothermal method and their in-vitro corrosion responses [J]. Surface and Coatings Technology, 2020, 394: 125858.

[8] DIKICI B, TOPUZ M. Production of annealed cold-sprayed 316L stainless steel coatings for biomedical applications and their in-vitro corrosion response [J]. Protection of Metals and Physical Chemistry of Surfaces, 2018, 54: 333−339.

[9] ZHOU J H, ZHAO L Z. Multifunction Sr, Co and F co-doped microporous coating on titanium of antibacterial, angiogenic and osteogenic activities [J]. Scientific Reports, 2016, 6: 29069.

[10] CLYNE T W, TROUGHTON S C. A review of recent work on discharge characteristics during plasma electrolytic oxidation of various metals [J]. International Materials Reviews, 2019, 64(3): 127−162.

[11] YIGIT O, OZDEMIR N, DIKICI B, KASEEM M. Surface properties of graphene functionalized TiO_2/nHA hybrid coatings made on Ti_6Al_7Nb alloys via plasma electrolytic oxidation (PEO) [J]. Molecules, 2021, 26(13): 3903.

[12] QADIR M, LI Y C, MUNIR K, WEN C E. Calcium phosphate-based composite coating by micro-arc oxidation (MAO) for biomedical application: A review [J]. Critical Reviews in Solid State and Materials Sciences, 2018, 43(5): 392−416.

[13] SONGUR F, DIKICI B, NIINOMI M, ARSLAN E. The plasma electrolytic oxidation (PEO) coatings to enhance in-vitro corrosion resistance of Ti−29Nb−13Ta−4.6Zr alloys: The combined effect of duty cycle and the deposition frequency [J]. Surface and Coatings Technology, 2019, 374: 345−354.

[14] MATYKINA E, ARRABAL R, SCURR D J, BARON A, SKELDON P, THOMPSON G E. Investigation of the mechanism of plasma electrolytic oxidation of aluminium using 18O tracer [J]. Corrosion Science, 2010, 52(3): 1070−1076.

[15] GAO Fang-yuan, HAO Li, LI Guang, XIA Yuan. The plasma electrolytic oxidation micro-discharge channel model and its microstructure characteristic based on Ti tracer [J]. Applied Surface Science, 2018, 431: 13−16.

[16] MORTAZAVI G, JIANG J, MELETIS E I. Investigation of the plasma electrolytic oxidation mechanism of titanium [J]. Applied Surface Science, 2019, 488: 370−382.

[17] AO N, LIU D X, ZHANG X H, HE G Y. Microstructural characteristics of PEO coating: Effect of surface nanocrystallization [J]. Journal of Alloys and Compounds, 2020, 823: 153823.

[18] RUDNEV V S, VASILYEVA M S, KONDRIKOV N B, TYRINA L M. Plasma-electrolytic formation, composition and catalytic activity of manganese oxide containing structures on titanium [J]. Applied Surface Science, 2005, 252(5): 1211−1220.

[19] WANG Shuai-xing, LIU Xiao-hui, YIN Xiao-le, DU Nan. Influence of electrolyte components on the microstructure and growth mechanism of plasma electrolytic oxidation coatings on 1060 aluminum alloy [J]. Surface and Coatings Technology, 2020, 381: 125214.

[20] CHANG L M. Growth regularity of ceramic coating on magnesium alloy by plasma electrolytic oxidation [J]. Journal of Alloys and Compounds, 2009, 468(1/2): 462−465.

[21] LI B, GUO Y H. Application of phase quantitative analysis in aluminum industry [J]. Physical Testing and Chemical Analysis (Part A: Physical Testing), 2011, 47: 217−221.

[22] NOMINÉ A, TROUGHTON S C, NOMINÉ A V, HENRION G, CLYNE T W. High speed video evidence for localised discharge cascades during plasma electrolytic oxidation [J]. Surface and Coatings Technology, 2015, 269: 125−130.

[23] TROUGHTON S C, NOMINÉ A, DEAN J, CLYNE T W. Effect of individual discharge cascades on the microstructure of plasma electrolytic oxidation coatings [J]. Applied Surface Science, 2016, 389: 260−269.

[24] STERN M, GEARY A L. Electrochemical polarization I. A

theoretical analysis of the shape of polarization curves [J]. Journal of the Electrochemical Society, 1957, 104(1): 56−63.
[25] FATIMAH S, YANG H W, KAMIL M P, KO Y G. Control of surface plasma discharge considering the crystalline size of Al substrate [J]. Applied Surface Science, 2019, 477: 60−70.
[26] BARATI DARBAND G, ALIOFKHAZRAEI M, HAMGHALAM P, VALIZADE N. Plasma electrolytic oxidation of magnesium and its alloys: Mechanism, properties and applications [J]. Journal of Magnesium and Alloys, 2017, 5: 74−132.
[27] HUSSEIN R O, NIE X, NORTHWOOD D O. An investigation of ceramic coating growth mechanisms in plasma electrolytic oxidation (PEO) processing [J]. Electrochimica Acta, 2013, 112: 111−119.
[28] CHEN W W, WANG Z X, SUN L, LU S. Research of growth mechanism of ceramic coatings fabricated by micro-arc oxidation on magnesium alloys at high current mode [J]. Journal of Magnesium and Alloys, 2015, 3(3): 253−257.
[29] PILLAI A M, RAJENDRA A, SHARMA A K. Influence of process parameters on growth behaviour and properties of coatings obtained by plasma electrolytic oxidation (PEO) on AA 6061 [J]. Journal of Applied Electrochemistry, 2018, 48: 543−557.
[30] ZHANG R F, ZHANG S F, SHEN Y L, ZHANG L H, LIU T Z, ZHANG Y Q, GUO S B. Influence of sodium borate concentration on properties of anodic coatings obtained by micro arc oxidation on magnesium alloys [J]. Applied Surface Science, 2012, 258(17): 6602−6610.
[31] WANG D D, LIU X T, WU Y K, HAN H P, YANG Z, SU Y, ZHANG X Z, WU G R, SHEN D J. Evolution process of the plasma electrolytic oxidation (PEO) coating formed on aluminum in an alkaline sodium hexametaphosphate ($(NaPO_3)_6$) electrolyte [J]. Journal of Alloys and Compounds, 2019, 798: 129−143.

磷酸盐和四硼酸盐电解质中阴离子对 Ti6Al4V 合金微弧氧化膜生长动力学的影响

王小明[1,2,3]，张福勤[1]

1. 中南大学 粉末冶金研究院，长沙 410083；
2. 邵阳学院 机械与能源工程学院，邵阳 422000；
3. 邵阳学院 高效动力系统智能制造湖南省重点实验室，邵阳 422000

摘　要：通过设计低含量 PO_4^{3-}和高含量 $B_4O_7^{2-}$离子电解液，采用扫描电镜、透射电镜、X 射线衍射和动电位极化等方法研究 Ti6Al4V 合金微弧氧化(MAO)涂层的生长动力学。结果表明，$B_4O_7^{2-}$离子提高放电火花强度，在高温下溶解大部分氧化物，在涂层/基态界面上形成较厚的阻挡层，从而提高涂层的极化电阻。低浓度 PO_4^{3-}离子促进微弧氧化涂层的均匀生长和外沉积层帽状孔洞的形成。在火花放电阶段，$Na_2B_4O_7$ 电解液中形成的 MAO 涂层厚度随时间呈指数增长，而在磷酸盐和四硼酸盐混合电解液中形成的 MAO 涂层厚度随 PO_4^{3-}离子含量的增加呈线性增长趋势。

关键词：Ti6Al4V 合金；微弧氧化；磷酸盐；四硼酸盐；电解液；阴离子；生长动力学

(Edited by Wei-ping CHEN)